Dynamical Contact Line Pinning and Zipping during Carbon Nanotube Coffee Stain Formation

Han Li,[†] Tilman C. Hain,[†] Andreas Muzha,[‡] Friedrich Schöppler,[†] and Tobias Hertel[†,§,*]

[†]Institute of Physical and Theoretical Chemistry, Faculty of Chemistry and Pharmacy, Julius-Maximilian University Würzburg, Am Hubland, 97074 Würzburg, Germany, [‡]Institute of Organic Chemistry, Faculty of Chemistry and Pharmacy, Julius-Maximilian University Würzburg, Am Hubland, 97074 Würzburg, Germany, and [§]Roentgen Research Center for Complex Material Systems, Julius-Maximilian University Würzburg, Am Hubland, 97074 Würzburg, Germany

ABSTRACT Thin films of single-wall carbon nanotubes (SWNTs) can be deposited onto solid substrates by evaporation-induced self-assembly. However, for this process to become more accessible to thin-film-based device fabrication requires optimization and a better understanding of the parameters and mechanisms governing nanoparticle film growth. Here, we focus on the role of contact-line (CL) dynamics at the edge of a receding meniscus for the deposition of thin nanoparticle films from colloidal suspensions. We find that film deposition rates can be increased by up to 2 orders of magnitude over earlier reports if parameters such as SWNT concentration, surfactant concentration, and height of the capillary bridge from which particles are deposited are properly adjusted. Most importantly we have also discovered that CL dynamics leading to the formation of striped films (coffee stains) are best described by dynamical pinning and kink-induced zipping. The existence of critical SWNT and surfactant concentrations as well as their role in determining stripe characteristics can be well accounted for by the proposed dynamical pinning and zipping model.

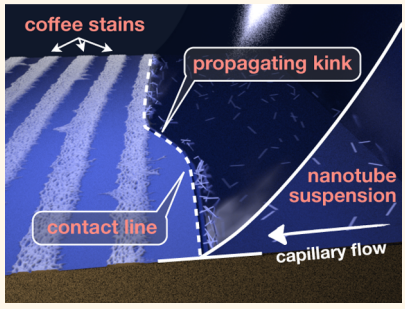

KEYWORDS: carbon nanotubes · coffee stain effect · evaporation-induced self-assembly · pinning · contact-line dynamics · thin films

The controlled deposition of nanoparticle films on solid substrates is essential for technologies such as inkjet printing,[1] the fabrication of functional coatings,[2,3] and nanoparticle-based electronic or photovoltaic devices as well as for sensors.[4−6] Single-wall carbon nanotubes (SWNTs) offer unique opportunities for use in applications bestowed onto them by nanoscale confinement.[7] However, even if individual SWNTs exhibit intriguing performance in devices such as single-nanotube field-effect transistors or light-emitting diodes,[8,9] they are perhaps more likely to find use as collectives of hundreds or thousands of nanotubes in thin films or other confined assemblies.[2−4,10,11] Ensembles generally allow for somewhat greater control of device properties due to averaging over fluctuations of material characteristics at the single-particle level. A greater realization of the potential of SWNTs for applications will thus rely on the development of versatile technologies for controlled nanotube thin film fabrication.[2]

Most efforts to fabricate thin SWNT films for applications have focused on techniques such as spin-coating, doctor-blading, or printing.[6,11,12] Recently, evaporation-induced self-assembly (EISA)[4,13] and the formation of so-called coffee stains by vertical deposition has also been explored for its use in the fabrication of structurally organized SWNT films.[4,11] The so-called pinning of the gas−solid−liquid contact line (CL) and its apparent stick−slip-type motion are generally considered key elements in understanding the formation of coffee stains.[14−18] However, the role of SWNT or surfactant concentrations as well as the rate of evaporation for CL dynamics as a key element of the mechanism underlying film formation has not been clarified sufficiently.[4,11,19] Moreover, the ability of the conventional stick−slip model in describing the formation of striped patterns during vertical deposition has been questioned before.[20]

RESULTS AND DISCUSSION

Here, we have investigated the nature of contact-line dynamics and its importance for determining the character of nanoparticle films deposited by evaporation-induced

* Address correspondence to tobias.hertel@uni-wuerzburg.de.

Received for review April 8, 2014 and accepted May 14, 2014.

Published online May 14, 2014
10.1021/nn501957y

self-assembly.[4,11,19] Key factors governing film structure such as rate of SWNT adsorption as well as the contrast between interfacial energies on bare and SWNT-covered surfaces at the CL can be controlled by SWNT and surfactant concentrations. We find that stripe formation can occur only above a certain critical SWNT concentration and is only observed within a narrow range of surfactant concentrations. In addition, CL pinning is found to be a dynamical process and cannot be properly described by sticking. Moreover, the advancement of the contact line is found to be facilitated by kink propagation and not by slippage of longer sections of a CL. We argue that the commonly discussed stick–slip process therefore misrepresents the key mechanism underlying the formation of nanoparticle coffee stains, which is best described by dynamical pinning and zipping.

The formation and structure of thin films on a SiO_2 substrate were here studied by electron and optical microscopy. Optical microscopy was found to be ideally suited to monitor CL dynamics by wide field imaging (see Figure 1a).[21,22] The SWNT suspensions from which films were deposited were highly enriched in the semiconducting (6,5) species by density gradient ultracentrifugation.[23] The two-plate setup used here provides superior stability during film formation if compared to evaporation from sessile droplets or by vertical deposition.[4,11] In Figure 2a we show optical images with a stripe pattern clearly emerging to the left of the CL. Automated video analysis could then be used to investigate CL dynamics under various conditions.

CL dynamics and film growth by EISA are here best discussed using the local geometry near the CL shown in Figure 1b. The solution of vapor transport equations over sessile droplets was previously shown by Deegan and co-workers to be associated with a vapor flux that diverges at the CL as $|\vec{j}| \propto r^{-(\pi-2\theta)/(2\pi-2\theta)}$, where r is the distance from the CL and θ is the contact angle.[15] As a result, solvent is drawn by capillary flow to the CL and sweeps suspended particles with it, which can then be deposited at the CL.[15] The resulting crowding of particles at the meniscus enables film formation—possibly accompanied by jamming[22]—and can lead to the deposition of some or all suspended particles at the edge of a droplet in the form of coffee stains.[18,24,25]

In Figure 2b we show contact-line dynamics as obtained from video sequences recorded for different capillary bridge heights d. The latter was adjusted by using spacers of different thickness. The observed dependence of the average CL velocity on the capillary bridge height is plotted in Figure 2c. The increasing CL velocity for small bridge heights d can be attributed to the aforementioned divergence of the evaporating flux at the CL. For the smallest spacer distances this leads to a CL velocity of over 2 $\mu m \cdot s^{-1}$, roughly 2 orders of magnitude higher than CL velocities reported previously.[4,11]

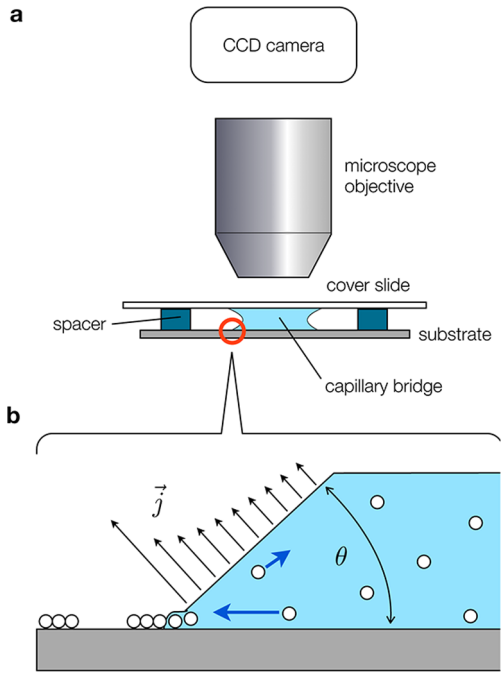

Figure 1. Experimental setup. (a) Microscope setup with two-plate geometry and capillary bridge. Video sequences are taken from the contact line (CL) on the bottom substrate. (b) Schematic illustration of the CL geometry, including vapor flux and capillary flow toward the CL.

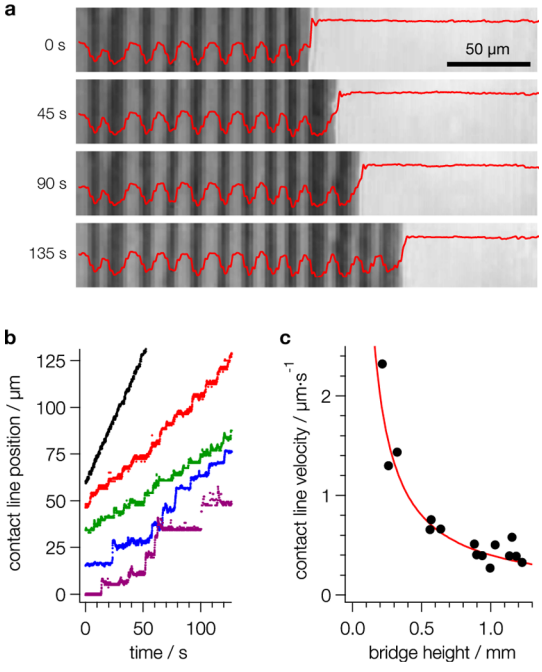

Figure 2. Video analysis of contact-line dynamics. (a) Video sequence of the advancing CL with a stripe pattern clearly emerging to the left. (b) CL dynamics for different capillary bridge heights indicate that the average CL velocity increases for small capillary bridge heights (top to bottom: 0.3 mm, 0.5 mm, 0.8 mm, 1.0 mm, 1.2 mm). (c) Measured average CL velocities increase dramatically at small bridge heights due to the diverging vapor flux at the CL.

Representative SEM images of SWNT films obtained for deposition from suspensions with different sodium

dodecyl sulfate (SDS) surfactant and SWNT concentrations are shown in Figure 3a. Over the range of concentrations studied here we observe four types of structures: (1) continuous films, (2) holey films, (3) striped films, and (4) spotty films. Spotty surfaces with islands made of SWNTs are found only at the lowest surfactant and SWNT concentrations. At somewhat higher SWNT and SDS concentrations we observe the formation of continuous films. SEM images also reveal that films as well as stripes consist of an entangled network of ordered SWNT filaments. The SWNT filaments have diameters between 5 and 10 nm as determined by atomic force microscopy (AFM) (see SI). Photoluminescence microscopy and spectroscopy discussed later moreover show that SWNTs within filaments retain their semiconducting characteristics.

The degree of local ordering within these films and stripes is expected to depend primarily on the rate at which SWNTs are deposited. Local order should improve if deposition rates are low.[11] Experiments by Yunker *et al*. moreover suggest that the formation of continuous films may be facilitated by capillary interactions between anisotropically shaped particles.[26] General scaling arguments[27] suggest that ordering of SWNTs can be expected if rotational and hydrodynamic time scales $\tau_r = (6D_r)^{-1}$ and $\tau_h = Lv^{-1}$ become similar. Here D_r is the rotational diffusion coefficient, L is the average particle distance in the suspension, and v is the velocity at which particles are swept to the CL. With a hydrodynamic radius of 5 nm,[28,29] D_r for 200 nm long SWNTs is on the order of 1 kHz, resulting in a critical hydrodynamic time scale of 0.16 ms. This imposes a limit of roughly 5 kHz on the rate at which SWNTs may self-align during deposition. Hydrodynamic forces near the CL may also facilitate self-organization.

In Figure 3b we show an overview of the range of SDS and SWNT concentrations over which the four major structural film types were studied. The striped phase is found only for deposition from SWNT suspensions with concentrations exceeding ~0.3×10^{-4} wt %. A nanotube concentration of 2.4×10^{-4} wt % here corresponds to an optical density of 1.0 at the first exciton subband transition at 982 nm measured for a 1 cm spectroscopy cell[30] (see SI). The range of SDS concentrations over which striped phases are observed is likewise limited to values between 0.05 and 0.15 wt %, shifting to slightly higher SDS concentrations as the SWNT concentration increases. No stripes are observed for SDS concentrations exceeding the critical micelle concentration (CMC) of 0.23 wt %.[31]

The mechanism of stripe formation is further investigated by comparison of SEM images (Figure 4a) with automated video analysis of CL dynamics as obtained from optical images (Figure 4b). The dynamics shown in Figure 4b at different surfactant concentrations, for example, show continuous CL movement at the lowest SDS concentration of 0.025 wt %, in agreement with the homogeneous films observed in SEM images. At intermediate SDS concentrations the CL dynamics

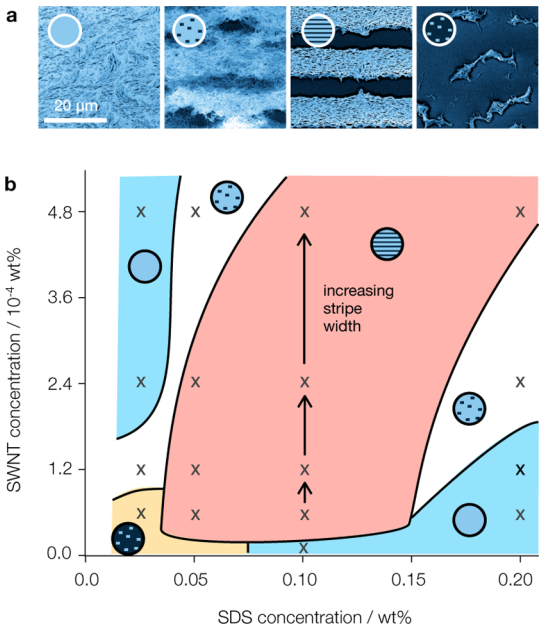

Figure 3. Structural phases observed during self-assembly of SWNT coffee stains. (a) SEM images with overview of observed phases: continuous, holey, striped, and spotty. (b) Schematic structural diagram as a function of SWNT and SDS concentrations obtained for a capillary bridge height of 550 μm and an average CL velocity of 0.3 $\mu m \cdot s^{-1}$. Crosses mark conditions for which SEM images have been obtained for film characterization (see SI).

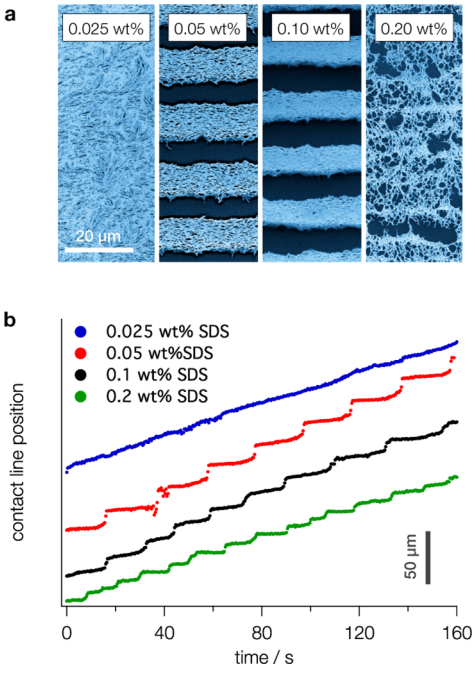

Figure 4. Observation of stripes from SEM images and video sequences. (a) Dependence of the film character on the SDS concentration for a fixed SWNT concentration ([SWNT] = 2.4×10^{-4} wt %) as observed by SEM. (b) CL dynamics for films grown under the same conditions as those in (a) as obtained from analysis of video sequences taken during film growth.

feature steps that are characteristic of the striped phase. At the highest SDS concentration of 0.20 wt % the CL dynamics in Figure 4b suggest that CL jumps still occur but become more frequent and less regular. The latter effect is practically impossible to discover from SEM images alone.

The most obvious trend within the striped phase is a gradual increase of its pitch from 9.5 μm to 24 μm and a concomitant increase of the stripe width from 2 μm to 15 μm with increasing SWNT concentration. The spacing between lines of 8 μm on the other hand remains roughly constant. The dependence of stripe pitch, width, and spacing on SWNT concentration is summarized in Figure 5 for an SDS concentration of 0.10 wt %.

The spacing between stripes can be analyzed by assuming that the advancement of the CL is sudden and not associated with any significant change of volume of the capillary bridge. The associated isochoric change of the contact angle $\Delta\theta$ can then be directly related to the CL slip distance Δx. For the parallel plate geometry this yields (see SI)

$$\Delta x = \frac{d}{4}\frac{\partial}{\partial\theta}\left\{\frac{\pi/2 - \theta - \cos\theta \sin\theta}{\cos^2\theta}\right\}\Delta\theta \qquad (1)$$

For contact angles in the vicinity of 15°, as measured for the bare substrate, this becomes $\Delta x \approx -d \times 0.0061 \times \Delta\theta$. With the observed CL slip distance of $\Delta x \approx 8$ μm this suggests that contact angle differences between the bare and SWNT-covered surfaces are only 2−3°. A similar approach has been used for analysis of MEH-PPV polymer stains for a sphere-on-flat geometry.[22]

Next, the range of SDS concentrations for which stripes exist can be analyzed by considering the dynamical effect that SWNT deposition has on the contact angle and CL position. The so-called pinning of the CL is generally discussed to be a prerequisite for stripe formation and is assumed to be initiated by deposition of nanoparticles at the CL. The specific circumstances under which pinning may occur, however, have remained somewhat unclear. The discussion of the slip distance between stripes has already shown that SWNT-covered surface areas must have a higher interfacial tension, which gives rise to a 2−3° smaller contact angle. By itself such a decrease of the contact angle would push the contact line further away from the capillary bridge. Evaporation on the other hand will pull the contact line toward the center of the capillary bridge. The onset of SWNT deposition is thus expected to lead to a dynamical interplay between decreasing contact angle and evaporation, both driving the CL in opposite directions. If the decrease of the contact angle due to SWNT deposition is sufficiently fast, it can offset the effect of solvent evaporation and decrease the CL velocity to zero. Under some conditions the CL may even reverse its direction of motion and become an advancing CL. Evidence for this can be taken from video sequences showing a subtle

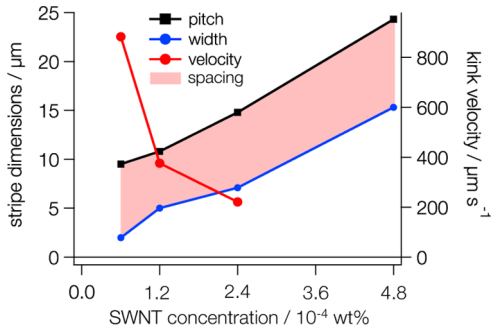

Figure 5. Stripe dimensions. Stripe width, pitch, spacing, and kink velocity as a function of SWNT concentration for an SDS concentration of 0.10 wt %, a capillary bridge height of 550 μm, and an average CL velocity of 0.3 μm·s^{-1}.

breathing motion of the CL (see scaled CL trace in Figure 6d). What is commonly referred to as pinning should thus be thought of as a dynamical process.

If we calculate the critical rate $d\theta/dt$ at which the contact angle must decrease to stop or reverse the receding CL motion, we obtain the following criterion for the two-plate geometry:

$$\frac{d\theta}{dt} \leq \frac{57.3°}{g(\theta)}\frac{v_{av}}{d} \qquad (2)$$

where $g(\theta) = (2\cos^2\theta)^{-1}\{(\pi/2 - \theta)\tan\theta - 1 - \cos^2\theta\}$ is a geometric function with a value of *ca.* −0.9 for the range of contact angles relevant to this study. v_{av} is the average contact line velocity as determined by the rate of evaporation, and d is the capillary bridge height. Dynamical pinning and the associated formation of stripes can then be directly related to the rate of change of the contact angle on SWNT-covered regions. For this rate to become sufficiently large we must have a sufficiently high SWNT concentration as well as a sufficiently high contrast of interfacial tensions between bare and SWNT-covered interface regions. Experimentally, the critical SWNT concentration for which the above criterion is fulfilled was found to be approximately 0.3×10^{-4} wt % (see Figure 3b).

Within the model discussed above we can now explain the absence of stripes at higher and at lower SDS concentrations by considering the dependence of the contrast in interfacial tensions on the SWNT-covered and bare surfaces. In Figure 6a we show a schematic illustration of bare and SWNT-covered substrate. Due to their hydrophobic character we expect the SWNTs to be covered with a larger concentration of SDS, irrespective of the bulk SDS concentration. A small number of SDS molecules will likely also assemble onto the hydrophilic substrate, but this concentration is expected to be lower than that on the SWNTs at all SDS bulk concentrations. This is illustrated schematically in Figure 6b by the expected qualitative dependencies of interfacial tensions on SWNT and bare substrate regions on the bulk SDS concentration. We speculate that an initial increase of the contrast (*i.e.*, difference)

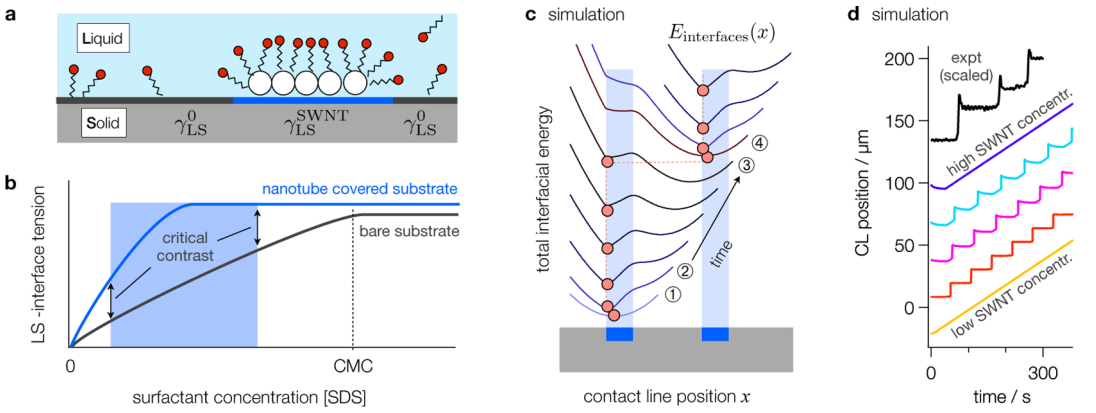

Figure 6. Mechanistic interpretation of contact line dynamics. (a) Schematic illustration of surfactant surface coverages on bare and SWNT-covered surface regions. (b) Schematic illustration of SDS-induced changes of interfacial tensions for bare and SWNT-covered substrate regions. At intermediate SDS concentrations we expect a large contrast of SDS surface coverage on bare and SWNT-covered surface regions and thus a large contrast of interfacial tensions. (c) Waterfall plot of calculated CL dynamics obtained from the development of interfacial energy contributions during film growth (see SI for details). (d) Waterfall plot. CL dynamics obtained from simulations at low, intermediate, and high SWNT concentrations qualitatively reproduce experimental observations. Of particular interest is the subtle breathing motion of the CL at higher SWNT concentrations, which can also be found in experimental CL traces (black line).

between the interfacial tensions for small SDS concentrations on both surfaces and eventually a decrease of this contrast at higher SDS concentrations defines the SDS concentration range within which stripes can be observed. No change in the contrast of interfacial tensions is expected for SDS concentrations beyond the CMC. These arguments also suggest that the critical SWNT concentration required for dynamical pinning and thus for stripe formation scales as $[SWNT]_{crit} \propto v_{av}d^{-1}$ (see SI).

To further explore the characteristics of stripe formation, we focus on CL dynamics as obtained from simple total energy calculations. This discussion is based on the simulation of the dependence of the total interfacial energy $E_{interfaces}$ on time t and CL position x similar to an approach used previously by Nonomura *et al.*[32]

$$E_{interfaces}(x) = E_{GS} + E_{SL} + E_{LG} \quad (3)$$

The relative contributions of different interfacial energies to eq 3 can be calculated using the difference of contact angles on bare and SWNT-covered substrate regions. This approach leaves the rate of SWNT deposition and the extent of the region over which SWNTs near the CL settle as the only free parameters for a simulation of CL dynamics (see SI). The edges of the deposition region are assumed to be slightly blurred. The width of the deposition region between 1 and 2 μm is obtained from the smallest stripe widths observed in our experiments. The qualitative behavior of the term $E_{interfaces}(x)$ as a function of time and CL position is shown in Figure 6c (see SI for details).

During the early stages of SWNT deposition, the spatial dependence of $E_{interfaces}$, in Figure 6c, develops a local minimum at the far side of the initial CL position and thus moves slightly outward (points 1 and 2 in Figure 6c). As mentioned above such a subtle breathing motion of the CL can also be observed experimentally (see black line in Figure 6d). The stripe at the dynamical pinning site matures as deposition of SWNTs continues and capillary forces increase. The local energy minimum eventually becomes metastable, and the CL slips to an advanced CL position (points 3 and 4 in Figure 6c). From there the process repeats itself. CL dynamics shown in Figure 6d are calculated within this model for different rates of SWNT deposition, *i.e.*, different SWNT concentrations. The simulations are characterized by a constant slip distance and a minor increase of the stripe width with deposition rate, *i.e.*, with SWNT concentration. However, the magnitude of the increase in stripe widths routinely falls short of experimental observations irrespective of the parameters used in the simulation.

The pronounced increase of the stripe width at higher SWNT concentrations thus remains the only experimental observation for which the simulations can not provide an explanation. In essence this suggests that the strains from capillary forces do not appear to rise as quickly as predicted by the simulations. Interestingly, however, we discovered that contact lines on striped surfaces generally do not advance by slippage[4,10,14,15,18,22,33] but rather by a zipper-type propagation of a kink defect (see Figure 7a).

Clear evidence for this can be seen in three video sequences included in the SI. Video sequences 1 and 2—slowed down by a factor of 4 for clarity—show that the formation of stripes is always accompanied by kink propagation in one or the other direction. The video sequences also show the formation of multiple kinks on the same line within the field of view as well as the fusion of kinks originating outside of the field of view but propagating toward one another (see video 1 at 0:14.7).

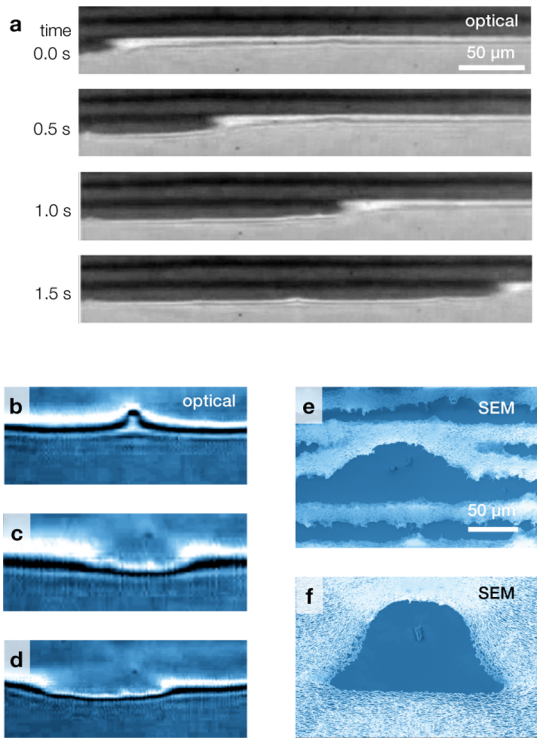

Figure 7. Contact line dynamics, kink propagation, and origins. (a) Video sequence showing the zipper-like movement of a kink from left to right. (b–d) Birth of two propagating kinks at an impurity. (e and f) SEM images of SWNT deposits near an impurity for striped and continuous films, respectively.

The third video sequence shows the formation of stripes from a coffee powder suspension and thereby illustrates the general nature of this phenomenon. For coffee suspensions the kinks are not as localized as in the SWNT case, but the propagation of transition regions is still clearly visible (see Figure 8a–c).

The zipper process can be thought of as a mechanism for providing relief from capillary strains on other sections of the CL. It thereby extends the time for which the CL stays on a maturing stripe and allows the stripe widths to continue to increase to the widths observed experimentally. Capillary strain relief by kinks in the CL can thus provide a simple explanation for the observation of broader stripe widths than predicted by simulations. The length scale of the kink perturbation of only a few tens of micrometers should be determined by a balance of capillary forces and the contrast of surface tensions between particle-covered and bare substrate regions. The velocity of kink propagation is found to be inversely proportional to critical length scales during stripe formation, as expected for a fixed evaporation rate (see Figure 5).

The video sequences feature several instances where the origin of kink propagation is within the field of view. Sometimes kinks appear to originate from an impurity site. This is seen in the sequence of video images in Figure 7b–d taken from video 1 starting at

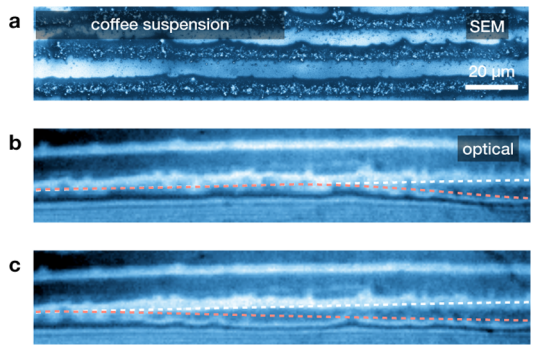

Figure 8. Contact-line dynamics during stripe formation from coffee suspensions. (a–c) Birth of a kink at an impurity.

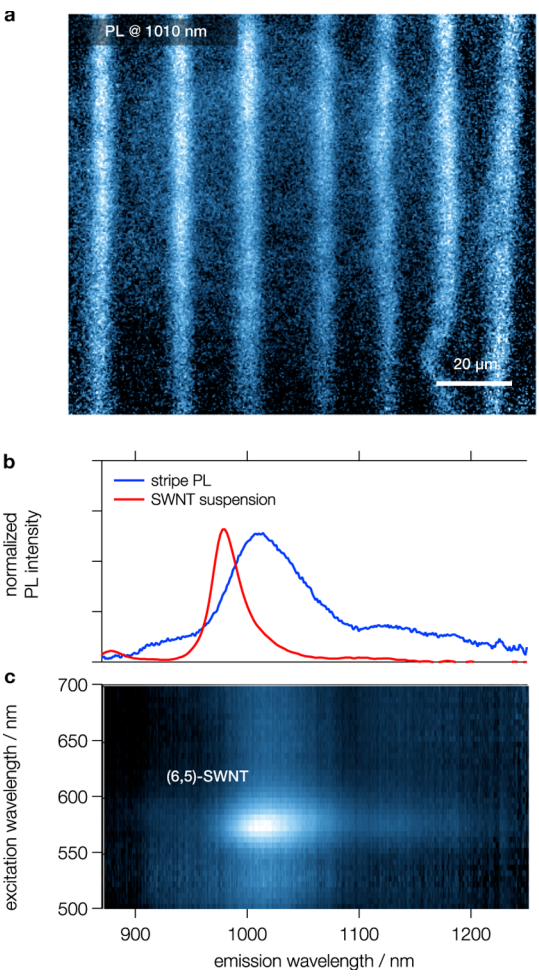

Figure 9. Fluorescence microscopy and spectroscopy of a self-assembled SWNT film. (a) Photoluminescence (PL) image of a stripe pattern recorded for emission from the first subband exciton. The sample is excited by 568 nm irradiation from a supercontinuum light source. (b) PL spectra from the starting material in suspension and the self-assembled film show a clear red-shift of emission on the substrate. (c) PL excitation spectrum of the same film reveals a broadened (6,5) PL emission feature.

0:47.3. As seen in SEM images, similar impurities are seen to leave a bell- or hat-shaped void on stripe and continuous film patterns (see Figure 7e and f). We infer from the width of these voids formed around

protruding impurities that the initial role of impurities is to provide local relief from capillary strains on the CL as the impurity starts to puncture the approaching liquid−gas interface. In some cases the video sequences also show the formation of multiple kinks on the same line. At other times the origin of kinks appears to be a seemingly featureless stripe region (video 1 starting at 0:07.6). With optical resolution, however, it is difficult to determine whether the origin of kink propagation in the latter cases is from a truly homogeneous region. Moreover, SEM images and the granular nature of nanoparticle stripes in general suggest that stripes are never perfectly uniform. Consequently, any stripe must feature some degree of heterogeneity of interfacial tension. Possible points of origin of kink propagation are thus either surface regions with higher capillary strains—as in the vicinity of defects—or regions with lower interfacial energies, for example if the density of adsorbed SWNTs is slightly lower. This implies that kink formation may be difficult and perhaps even fundamentally impossible to avoid.

Lastly, we have also investigated the optical properties of self-assembled stripe structures by fluorescence microscopy and fluorescence excitation spectroscopy. The photoluminescence (PL) image of a surface covered by a striped SWNT pattern in Figure 9a clearly demonstrates that the self-assembled SWNT filaments in these structures preserve the semiconducting character of the starting SWNT material. The PL spectra and the PL excitation spectrum in Figure 9b and c, however, also show that interactions among SWNTs and possibly with the underlying substrate also lead to a considerable red-shift of emission features.

The process of stripe self-organization can also be repeated to fabricate more complex structures.[34] A sequential deposition of stripes or continuous films on top of one another is made possible by appropriate choice of SDS and SWNT concentrations following the insights provided by the above discussion (see Figure 10).

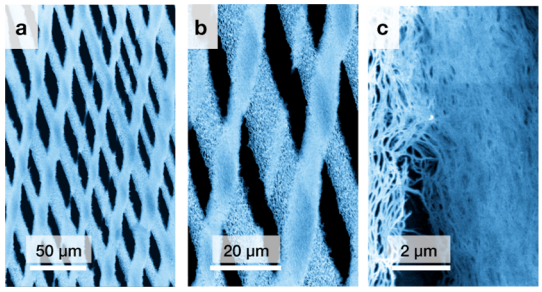

Figure 10. Sequential stripe deposition. (a−c) SEM images obtained for increasing magnification of a diamond-shaped double-stripe pattern.

CONCLUSIONS

In conclusion, we have investigated the mechanism underlying the formation of different film types by EISA from SWNT suspensions. We find that the rate of film deposition can be increased by at least 2 orders of magnitude over earlier attempts by using a narrowly spaced two-plate geometry for deposition. CL dynamics are key to the formation of striped or continuous films. We have found that stripe patterns (or coffee stains) can be formed within a critical range of SWNT and surfactant concentrations. The commonly used concept of CL pinning was found to be a dynamical process that reflects the interplay of sufficiently rapid buildup of a contrast in interfacial tensions at the CL and capillary strains. Surfactant and nanotube concentrations can thus be used as parameters for controlling film formation. In addition, the advancement of the CL was discovered to be by zipper-like kink propagation, which allows relieving capillary strains. The commonly implied stick−slip phenomenon in discussing coffee stain formation thus seems to be misleading. The notion of dynamical pinning and kink-induced strain relief appears to more adequately describe the actual mechanisms governing stripe formation in EISA. The insights provided here may open new opportunities for thin SWNT film fabrication by EISA.

METHODS

Sample Preparation. Aqueous colloidal suspensions of SDS-stabilized SWNTs (CoMoCAT SG65, SWeNT SouthWest Nanotechnologies) were obtained by dialysis from density gradient ultracentrifugation samples fabricated using the procedure described by Bergler *et al.*[35] Si wafers (MicroChemicals) and glass cover slides (Paul Marienfeld GmbH & Co. KG) were cleaned with a 2:1 mixture of 98% sulfuric acid and 30% hydrogen peroxide. Before use, slides were rinsed with HPLC water and blown dry with N_2. For the EISA process we placed *ca.* 40 μL of SWNT suspension between the Si substrate and a cover slide. Solvent evaporation proceeded at room temperature and atmospheric pressure. Unless noted otherwise the average CL velocity was 0.2 $\mu m \cdot s^{-1}$.

The setup shown for EISA in Figure 1a provides superior stability and control of growth conditions because the small gas−solvent surface area increases the frequency of surface waves, which thereby decouples the system from low-frequency environmental perturbations.

Sample Characterization and CL Dynamics. The dynamics of the CL were observed by optical microscopy (BX41, Olympus) using a Spindler & Hoyer objective (10×/0.3 N.A.). Video sequences were recorded with 720 × 576 pixel resolution at 25 fps. A field emission SEM (Ultra Plus, Carl Zeiss) was used to investigate the microscopic structure of SWNT films. Image analysis was carried out with the Igor Pro software package (Wavemetrics Inc.). AFM images were obtained with Nanosurf Easyscan 2 (Nanosurf GmbH) in the tapping mode using Tap190Al-G tips (Budget Sensors).

For PL imaging, we used an interline CCD camera (Clara, Andor), attached to an inverted epi-fluorescence microscope (Ti−U, Nikon), with a CFI Super Plan objective (20×/0.45 N.A., Nikon). PLE mapping was conducted on a home-built setup, based on a Shamrock spectrograph (SR-303i, Andor) and an

InGaAs array detector (iDus, Andor). Excitation was accomplished by a supercontiuum light source, supplied with a variable band-pass filter (SuperK Extreme EXR-15 & SuperK Varia, NKT Photonics).

Conflict of Interest: The authors declare no competing financial interest.

Acknowledgment. H.L. acknowledges a scholarship by the Chinese Scholarship Council.

Supporting Information Available: Sample characterization, theoretical model, and simulation. This material is available free of charge *via* the Internet at http://pubs.acs.org.

REFERENCES AND NOTES

1. Sirringhaus, H.; Kawase, T.; Friend, R. H.; Shimoda, T.; Inbasekaran, M.; Wu, W.; Woo, E. P. High-resolution Inkjet Printing of All-Polymer Transistor Circuits. *Science* **2000**, *290*, 2123–2126.
2. Cao, Q.; Rogers, J. A. Ultrathin Films of Single-Walled Carbon Nanotubes for Electronics and Sensors: A Review of Fundamental and Applied Aspects. *Adv. Mater.* **2009**, *21*, 29–53.
3. Hammond, P. T. Form and Function in Multilayer Assembly: New Applications at the Nanoscale. *Adv. Mater.* **2004**, *16*, 1271–1293.
4. Engel, M.; Small, J. P.; Steiner, M.; Freitag, M.; Green, A. A.; Hersam, M. C.; Avouris, P. Thin Film Nanotube Transistors Based on Self-Assembled, Aligned, Semiconducting Carbon Nanotube Arrays. *ACS Nano* **2008**, *2*, 2445–2452.
5. Martel, R. Sorting Carbon Nanotubes for Electronics. *ACS Nano* **2008**, *2*, 2195–2199.
6. Bindl, D. J.; Wu, M. Y.; Prehn, F. C.; Arnold, M. S. Efficiently Harvesting Excitons from Electronic Type-Controlled Semiconducting Carbon Nanotube Films. *Nano Lett.* **2011**, *11*, 455–460.
7. Avouris, P.; Chen, Z. H.; Perebeinos, V. Carbon-Based Electronics. *Nat. Nanotechnol.* **2007**, *2*, 605–615.
8. Chen, J.; Perebeinos, V.; Freitag, M.; Tsang, J.; Fu, Q.; Liu, J.; Avouris, P. Bright Infrared Emission from Electrically Induced Excitons in Carbon Nanotubes. *Science* **2005**, *310*, 1171–1174.
9. Martel, R.; Schmidt, T.; Shea, H. R.; Hertel, T.; Avouris, P. Single- and Multi-wall Carbon Nanotube Field-Effect Transistors. *Appl. Phys. Lett.* **1998**, *73*, 2447–2449.
10. Han, W.; Lin, Z. Q. Learning from "Coffee Rings": Ordered Structures Enabled by Controlled Evaporative Self-Assembly. *Angew. Chem., Int. Ed.* **2012**, *51*, 1534–1546.
11. Shastry, T. A.; Seo, J. W. T.; Lopez, J. J.; Arnold, H. N.; Kelter, J. Z.; Sangwan, V. K.; Lauhon, L. J.; Marks, T. J.; Hersam, M. C. Large-Area, Electronically Monodisperse, Aligned Single-Walled Carbon Nanotube Thin Films Fabricated by Evaporation-Driven Self-Assembly. *Small* **2013**, *9*, 45–51.
12. Beyer, S.; Walus, K. Controlled Orientation and Alignment in Films of Single-Walled Carbon Nanotubes Using Inkjet Printing. *Langmuir* **2013**, *28*, 8753–8759.
13. Brinker, C. J.; Lu, Y. F.; Sellinger, A.; Fan, H. Y. Evaporation-Induced Self-Assembly: Nanostructures Made Easy. *Adv. Mater.* **1999**, *11*, 579.
14. Adachi, E.; Dimitrov, A. S.; Nagayama, K. Stripe Patterns Formed on a Glass-Surface during Droplet Evaporation. *Langmuir* **1995**, *11*, 1057–1060.
15. Deegan, R. D.; Bakajin, O.; Dupont, T. F.; Huber, G.; Nagel, S. R.; Witten, T. A. Capillary Flow as the Cause of Ring Stains from Dried Liquid Drops. *Nature* **1997**, *389*, 827–829.
16. Morales, V. L.; Parlange, J. Y.; Wu, M. M.; Perez-Reche, F. J.; Zhang, W.; Sang, W. J.; Steenhuis, T. S. Surfactant-Mediated Control of Colloid Pattern Assembly and Attachment Strength in Evaporating Droplets. *Langmuir* **2013**, *29*, 1831–1840.
17. Nagayama, K. Two-Dimensional Self-Assembly of Colloids in Thin Liquid Films. *Colloids Surf., A* **1996**, *109*, 363–374.
18. Snoeijer, J. H.; Andreotti, B. Moving Contact Lines: Scales, Regimes, and Dynamical Transitions. *Annu. Rev. Fluid Mech.* **2013**, *45*, 269–292.
19. Small, W. R.; Walton, C. D.; Loos, J.; Panhuis, M. I. H. Carbon Nanotube Network Formation from Evaporating Sessile Drops. *J. Phys. Chem. B* **2006**, *110*, 13029–13036.
20. Watanabe, S.; Inukai, K.; Mizuta, S.; Miyahara, M. Mechanism for Stripe Pattern Formation on Hydrophilic Surfaces by Using Convective Self-Assembly. *Langmuir* **2009**, *25*, 7287–7295.
21. Kim, B. H.; Shin, D. O.; Jeong, S. J.; Koo, C. M.; Jeon, S. C.; Hwang, W. J.; Lee, S.; Lee, M. G.; Kim, S. O. Hierarchical Self-Assembly of Block Copolymers for Lithography-Free Nanopatterning. *Adv. Mater.* **2008**, *20*, 2303.
22. Xu, J.; Xia, J. F.; Hong, S. W.; Lin, Z. Q.; Qiu, F.; Yang, Y. L. Self-Assembly of Gradient Concentric Rings via Solvent Evaporation from a Capillary Bridge. *Phys. Rev. Lett.* **2006**, *96*, 066104.
23. Arnold, M.; Green, A.; Hulvat, J.; Stupp, S.; Hersam, M. Sorting Carbon Nanotubes by Electronic Structure Using Density Differentiation. *Nat. Nanotechnol.* **2006**, *1*, 60–65.
24. Deegan, R. D.; Bakajin, O.; Dupont, T. F.; Huber, G.; Nagel, S. R.; Witten, T. A. Contact Line Deposits in an Evaporating Drop. *Phys. Rev. E* **2000**, *62*, 756–765.
25. Huber, G. Rush Hour in a Drop of Coffee. *Physics* **2011**, *4*, 65.
26. Yunker, P. J.; Still, T.; Lohr, M. A.; Yodh, A. G. Suppression of the Coffee-Ring Effect by Shape-Dependent Capillary Interactions. *Nature* **2011**, *476*, 308–311.
27. Marin, A. G.; Gelderblom, H.; Lohse, D.; Snoeijer, J. H. Order-to-Disorder Transition in Ring-Shaped Colloidal Stains. *Phys. Rev. Lett.* **2011**, *107*, 085502.
28. Arnold, M. S.; Suntivich, J.; Stupp, S. I.; Hersam, M. C. Hydrodynamic Characterization of Surfactant Encapsulated Carbon Nanotubes Using an Analytical Ultracentrifuge. *ACS Nano* **2008**, *2*, 2291–2300.
29. Hertel, T.; Himmelein, S.; Ackermann, T.; Stich, D.; Crochet, J. Diffusion Limited Photoluminescence Quantum Yields in 1-D Semiconductors: Single-Wall Carbon Nanotubes. *ACS Nano* **2010**, *2*, 7161–7168.
30. Schöppler, F.; Mann, C.; Hain, T. C.; Neubauer, F. M.; Privitera, G.; Bonaccorso, F.; Chu, D. P.; Ferrari, A. C.; Hertel, T. Molar Extinction Coefficient of Single-Wall Carbon Nanotubes. *J. Phys. Chem. C* **2011**, *115*, 14682–14686.
31. Paula, S.; Siis, W.; Tuchtenhagen, J.; Blume, A. Thermodynamics of Micelle Formation as a Function of Temperature: A High Sensitivity Titration Calorimetry Study. *J. Phys. Chem.* **1995**, *99*, 11742–11751.
32. Nonomura, M.; Kobayashi, R.; Nishiura, Y.; Shimomura, M. Periodic Precipitation during Droplet Evaporation on a Substrate. *J. Phys. Soc. Jpn.* **2003**, *72*, 2468–2471.
33. Cazabat, A. M.; Guena, G. Evaporation of Macroscopic Sessile Droplets. *Soft Matter* **2010**, *6*, 2591–2612.
34. Mino, Y.; Watanabe, S.; Miyahara, M. Fabrication of Colloidal Grid Network by Two-Step Convective Self-Assembly. *Langmuir* **2011**, *27*, 5290–5295.
35. Bergler, F. F.; Schöppler, F.; Brunecker, F. K.; Hailman, M.; Hertel, T. Fluorescence Spectroscopy of Gel-Immobilized Single-Wall Carbon Nanotubes with Microfluidic Control of the Surfactant Environment. *J. Phys. Chem. C* **2013**, *117*, 13318–13323.